Supplementary Information

A novel $Ba_{0.5}Sr_{0.5}Co_{0.8}Fe_{0.2}O_{3-\delta}$ and CeO_2 hybrid electrocatalyst for both oxygen evolution and methanol oxidation reactions

Fuyue Liu[‡, a], Fei Wu[‡, b], Ran Guo[c], Jiaxin Dang[a], Haoqi Qiu[a], Qiuju Zhang[b, *], Chao Yang[c], He Miao[a, *], Jinliang Yuan[a]

[a] Faculty of Maritime and Transportation, Ningbo University, Ningbo 315211, PR China

[b] Ningbo Institute of Materials Technology and Engineering, Chinese Academy of Sciences, Ningbo, 315211, PR China

[c] Shanghai Frontiers Science Center of "Full penetration" far-reaching offshore ocean energy and power, Merchant Marine College, Shanghai Maritime University, Shanghai 200135, China

[*] Corresponding author:

Prof. Qiuju Zhang, E-mail: zhangqj@nimte.ac.cn

Prof. He Miao, E-mail: miaohe@nbu.edu.cn

‡ These authors contributed equally to this work

■ Chemicals

$Ba(NO_3)_2$, $Sr(NO_3)_2$, $Fe(NO_3)_3 \cdot 9H_2O$, $Co(NO_3)_2 \cdot 6H_2O$, ethylenediaminetetraacetic acid (EDTA, $C_{10}H_{16}N_2O_8$), citric acid (CA, $C_6H_8O_7$), ethanol, RuO_2, 20 wt.% Pt/C and KOH were purchased from Aladdin Ltd. $Ce(NO_3)_2 \cdot 6H_2O$, NaOH, methanol and potassium formate (HCOOK) were purchased from Shanghai Yongchuan Biotechnology Co., Ltd. . Conductive carbon (VXC-72) was purchased from Cabot Ltd.. Nafion solution (5 wt.%, 80 μL) was sourced from DuPont Ltd. Carbon cloth (CC) was sourced from CeTech Co., Ltd. The water used in this experiment was deionized (DI) water (> 18.0 MΩ·cm). The above reagents were analytical grade (AR) and purchased from commercial channels without further processing unless otherwise specified. Both CPAM and TMAOH used in this work are experimental grade purity and purchased from Baichuan Biotechnology Co., Ltd., Ningbo, China.

■ Preparation of materials

The pristine $Ba_{0.5}Sr_{0.5}Co_{0.8}Fe_{0.2}O_{3-\delta}$ (BSCF) powder sample was prepared by a classical sol-gel method, and the CeO_2 powder was synthesized by simple precipitation method. For preparation of BSCF, the stoichiometric ratios of $Ba(NO_3)_2$, $Sr(NO_3)_2$, $Co(NO_3)_3 \cdot 6H_2O$ and $Fe(NO_3)_3 \cdot 9H_2O$ (total metal ions, 20 mmol) were dissolved into 250 mL deionized (DI) water followed by adding citric acid (CA) and ethylenediaminetetraacetic acid (EDTA). The total mole of metal ions: CA: EDTA = 1: 2.5: 0.5, and the pH value of the mixture was adjusted to about 6 with $NH_3 \cdot H_2O$. Next, the mixture was vigorously stirred at the temperature of 80 ℃. After the gel formed, dry it at 180 °C for 10 hours in air. Subsequently, the dry gel was sintered at 950 °C for 5 hours with a heating rate of 100 °C h^{-1}. Finally, the obtained powder was the pristine BSCF.

For the preparation of CeO_2 powder, NaOH was added into the aqueous solution with a certain concentration of $Ce(NO_3)_2 \cdot 6H_2O$ to form the precipitate of $Ce(OH)_3$, and then the precipitate was centrifuged and filtered three times with DI water and ethanol, and dried in an oven at 80 ℃. Finally, the above dried samples were sintered at 800 ℃

for 2 h in a muffle furnace with a heating rate of 100 ℃ h^{-1} to obtain the pristine CeO_2 powder.

For preparing the BSCF@CeO_2 hybrid, the BSCF powder (0.50 mmol, 0.110 g) was placed in 100 mL of deionized (DI) water and stirred magnetically at 200 rpm. Then, slowly drop 100 mL of the transparent solution formed by dissolving 0.060 g cationic polyacrylamide (CPAM) in 100 mL DI water followed by the magnetic stirring for 1 h. After centrifugal filtration, the product was added into 100 mL DI water and heated at 50 ℃ in a water bath to form solution A. Subsequently, the two solutions of x/100 mmol/L (x=5, 10, 15, 20, 30, 40) $Ce(NO_3)_2 \cdot 6H_2O$ and 3.3x/100 mmol/L (x=5, 10, 15, 20, 30, 40) NaOH were simultaneously added dropwise in the solution A. During the additions of $Ce(NO_3)_2 \cdot 6H_2O$ and NaOH solutions, the PH value of solution A maintained about 9.5. Then, the precipitated product was centrifugally filtered with DI water and ethanol for three times, and dried at 100 ℃ for 10 h. Finally, the dried product was sintered at 800 ℃ for 2 h in a muffle furnace with a heating rate of 100 ℃/h to obtain the composite product BSCF@CeO_2-x (x=5, 10, 15, 20, 30 and 40). Solution A without addition of $Ce(NO_3)_2 \cdot 6H_2O$ and NaOH solutions followed by centrifugal cleaning and drying at 80 ℃ for 10 h in oven was named as BSCF@CPAM.

The control sample of BSCF+CeO_2-10 was synthesized by simply grinding and mixing the synthesized pristine BSCF and CeO_2 powders according to the molar ratio of 5: 1 at the ambient temperature. BSCF-CeO_2-10 was synthesized with the same method of BSCF@CeO_2-10 except for the addition of CPAM. The pristine BSCF powder was sintered at 800℃ for 2h in a muffle furnace with a heating rate of 100 ℃/h to yield another control sample of BSCF-800.

■ Material characterizations

X-ray diffraction (XRD) patterns were obtained on a Bruker D8 Advance X-ray diffract meter (Cu Kα=1.5418 Å) at a scanning rate of 0.02° s^{-1} from 20° to 90°. The microstructures of the synthesized samples were observed using a field-emission scanning electron microscopy (FESEM, Hitachi S4800, 5kV). Transmission electron

microscopy (TEM) and high-resolution TEM (HR-TEM) images of the as-prepared samples were observed by transmission electronic microscopy (TEM, JOEL JEM-2100). X-ray photoelectron spectroscopy (XPS) data were obtained on an AXISULTARDLD spectroscopy spectrometer with an Al-Kα X-ray source. Nuclear magnetic resonance (NMR) spectra are carried out by Bruker AVANCE III HD 600 MHz (Germany). Before measurement, the measured alkaline solutions are neutralized by 2.0 M H_2SO_4 to keep the pH value of 8.

■ Preparation of the working electrodes

The preparation method of the catalyst ink was described as the follows according to our previous work [1]. 5 mg catalyst and 5 mg carbon (Vulcan-XC72) were dispersed in 2.0 mL ethanol plus 80 μL of 5 wt.% Nafion solution and ultrasonically blended for 0.5 h to form a well-dispersed ink. Then, 20 μL of the ink was pipetted on a polished glassy carbon (GC) electrode for preparation of working electrode, and the solvent was evaporated naturally with a catalyst loading of ~0.245 mg cm^{-2}.

■ Electrochemical measurements

For measuring the working electrode, oxygen with ultrahigh purity grade was bubbled into the electrolyte to make it O_2-saturated during the measurements. The electrochemical performances of the working electrodes were measured by the standard three-electrode system (the above working electrode, the counter electrode of carbon rod provided by Shanghai Ledun Industrial Co., Ltd and the reference electrode of Hg/HgO (1 M NaOH) electrode provided by CHI Instruments, Inc) by rotating disc electrode (RDE, PINE) with the area of 0.196 cm^2 and CHI 760E electrochemical workstation (Shanghai Chenhua, China) in 1 M KOH under a rotating speed of 1600 rpm.

Linear sweep voltammetry (LSV) was recorded from 0.2 to 1.0 V vs. Hg/HgO at a scan rate of 5 mV s^{-1}. Electrochemical impedance spectrum (EIS) was measured at 1.523 V vs. RHE over a frequency range from 10^5 to 0.1 Hz. The equation: $\eta = E_{RHE}$-1.23 V was adopted to calculate the overpotentials (η) of the working electrodes. The Tafel equation ($\eta = b\log j + a$) was adopted to calculate the Tafel slopes, where η is the

overpotential, j represents current density, and b is the Tafel slope [2]. The electrochemically active surface area (ECSA= C_{dl}/C_s) was assessed by measuring double-layer capacitance (C_{dl}) from CV with different scanning rates. C_S represents the specific capacitance of 1.0 M KOH (0.04 mF cm^{-2}) [2]. The C_{dl} which was positively correlated to the ECSA was assessed by $C_{dl} = j_c/V$, where j_c represented the current density, and V was the voltage measured by CV. The scanning potential range was from 0.132 to 0.232 V (vs. Hg/HgO) at scan rates of 10, 20, 30, 40, 50, 60, 70, 80, 90 and 100 mV s^{-1} in 1 M KOH solution. By drawing the curve of Δj ($\Delta j = 0.5\ (j_{anode} - j_{cathode})$) against the scanning rate, the slope of the fitting line indicated the C_{dl}. The measured potentials were converted into potentials vs. RHE by the Nernst equation ($E_{(RHE)} = E_{(Hg/HgO)} + 0.098 + 0.059 \times pH$). In addition, the equation ($E_C = E_M - i\,R_s$) was adopted to correct the compensated potential, where R_s is the ohmic solution resistance measured by EIS, i is the current, E_C is the correction voltage and E_M is the measurement voltage. The stability tests of the catalysts were performed by the Chronopotentiometry (CP) method at j=10 mA cm^{-2}.

■ Overall water splitting measurements

The anodes for overall water (alkaline water, alkaline simulated seawater and alkaline natural seawater) splitting (OWS) were prepared by the as-prepared catalyst coated on Ni foam (NF, 1 cm x 1 cm x 1.5 mm) with the total catalyst load being about 2.0 mg cm^{-2}. The cathode was the commercial 20 wt.% Pt/C which was dripped onto NF with the total load of about 2.0 mg cm^{-2}. The stability tests of OWS were performed at the current density of 10 mA cm^{-2} in alkaline aqueous solution, alkaline simulated seawater and alkaline natural seawater (taken from the East China Sea, 29°52'00.00"N, 121 °31'00.00"E) [3]. All the OWS stability tests were evaluated by the uncompensated resistance. In our work, the simulation seawater was 0.5 M NaCl solution. The alkaline nature seawater in our paper was the mixed solution of nature seawater with 1 M KOH.

■ Oxygen intercalation and diffusion coefficient measurements

The electrochemical oxygen intercalation/deintercalation were performed in Ar-

saturated 1 M KOH solution at ambient temperature using a catalyst-coated GC working electrode with a carbon rod as the counter electrode and a Hg/HgO as the reference electrode. CV was conducted at 20 mV s^{-1} scan rate with the working electrode being stationary. To measure the oxygen ion diffusion coefficient, chronoamperometry was performed on the same working electrode by applying a potential being 50 mV more than $E_{1/2}$ which was defined as the average potential of oxygen intercalation/deintercalation in CV curves. The RDE's rotation rate was 1600 rpm during the chronoamperometry test to remove any electrolyte-based mass-transfer effects. The chronoamperometry data were plotted as current vs. the inverse square root of time (i vs. $t^{-1/2}$), in which the linear portion was fitted to obtain the intercept with the $t^{-1/2}$ axis (at $i = 0$). Using a bounded 3D diffusion model [4, 5], this intercept was used to calculate the oxygen ion diffusion coefficient (D_O) according to the equation $\lambda = a(D_O t)^{-1/2}$, where λ was a dimensionless shape factor, a was the radius of the particle. Here, λ was assumed to be 2, which was representative of a rounded parallelepiped, halfway between the values for a sphere ($\lambda = 1.77$) and a cube ($\lambda = 2.26$). a was 28 μm estimated from statistics analysis based on their SEM images.

■ Molecular dynamics modeling method

A molecular dynamics (MD) modeling method was applied to predict the sintering process and microstructures of BSCF@CeO_2-10. The MD model was implemented on the Large Scale Atomic / Molecular Parallel Simulator (LAMMPS) to describe the co-sintering processes of the BSCF's cuboid matrix and CeO_2 nanoparticles systems [6]. In addition, the MD simulation method with the core (for BSCF)-shell (for CeO_2) model was employed to predict the particle interaction of BSCF@CeO_2-10 cuboid in the co-sintering process, which incorporated the polarizability of charged particles in terms of a pair of the charged core and shell linked with a harmonic spring interaction in the individual atom. It should be noted that we only approximated the MD variation of the pristine BSCF with a rectangular cuboid-like simulated structure. Also, the core-shell model was appropriated to describe the stable trajectories of the particles in the crystalline materials with high symmetric locations for each core-shell pair [7].

What's more, the MD simulation method was sintered at the isothermal-isobaric canonical ensemble (NPT) ensemble under 1073 K and 0.1 MPa for 1 ns, and further equilibrated at the isothermal-isometric canonical ensemble (NVT) for a while to obtain the sintered structure.

The crystal lattice parameters of BSCF and CeO_2 predicted in the current work were compared with the experimental or theoretical data for the modeling validation. The BSCF crystal supercell was built with 2880 atoms in total, in which 320 Ba atoms, 320 Sr atoms, 512 Co atoms, 128 Fe atoms and 1600 O atoms were included. The supercell model was sintered at an isothermal-isobaric canonical ensemble (NPT) under 1073 K and 0.1 MPa for 300 ps, which was cooled down to the room temperature and equilibrated for 50 ps to obtain the sintered structure.

As shown in **Tab. S3**, the predicted lattice parameter of BSCF cuboid matrix is 4.010 Å, which is agreed well with the lattice parameter of 3.982 Å demonstrated by the XRD experimental results in **Tab. S1**. Moreover, the maximum relative error of the simulated parameters is less than 5%. Similarly, a crystal supercell model of CeO_2 was built with 6264 atoms in total, in which 2088 Ce atoms and 4176 O atoms were included.

Ultimately, the BSCF@CeO_2-10 cuboid matrix composite system was modeled with 194,508 particles in total. The final state sintered structure was obtained under the same conditions as for the sintering procedures presented above.

In fact, the compressive stress induced by the loading of CeO_2 particles on the BSCF can lead to the compression of the BSCF cell volume during the MD simulation. In other words, the generated compressive stress causes the compressive strain of the BSCF cells. Therefore, there is a close correlation between compressive stress and compressive strain.

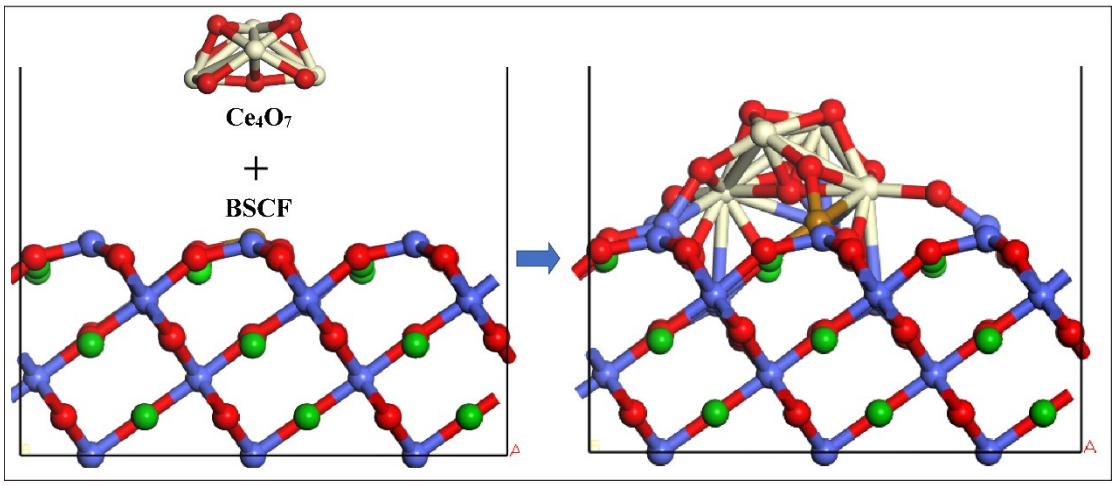

Fig. S1 Atomic structures of BSCF and BSCF@CeO_2.

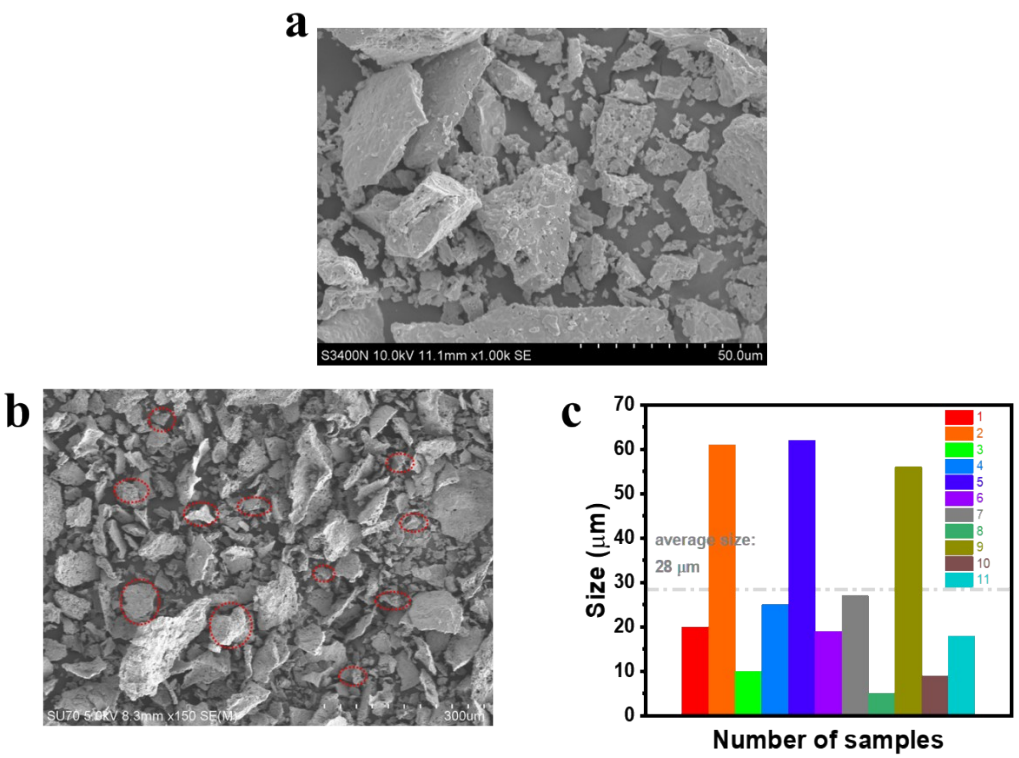

Fig. S2 SEM images of BSCF (a) and BSCF@CeO_2-10 (b) under low magnification, and average particle size estimation of BSCF@CeO_2-10 (c).

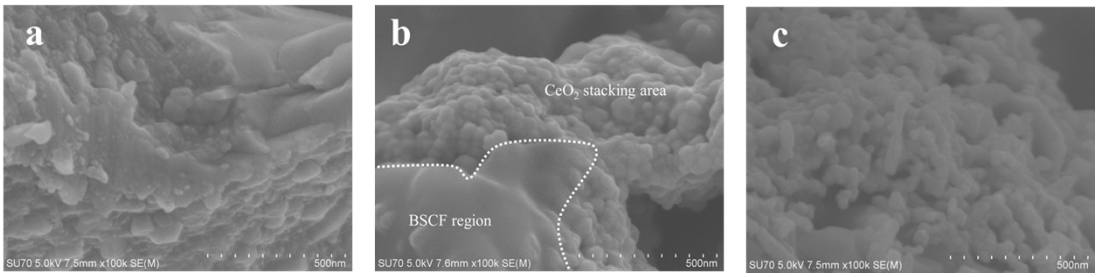

Fig. S3 SEM images of BSCF@CeO_2-5 (a), BSCF@CeO_2-20 (b) and BSCF@CeO_2-40 (c).

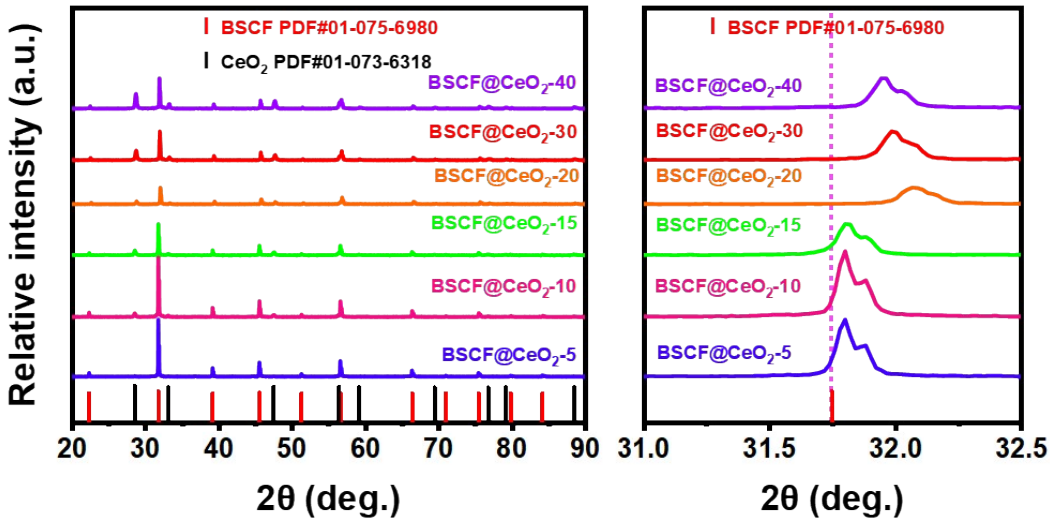

Fig. S4 XRD patterns of BSCF@CeO_2-x (x=5, 10, 15, 20, 30, 40) and the local magnification at 31.0~32.5 ° .

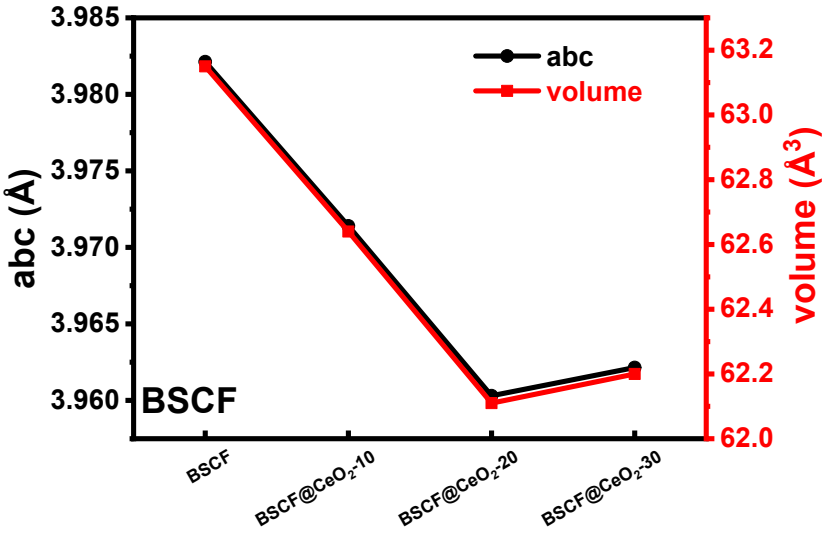

Fig. S5 Cell parameters and volumes (V) of BSCF phase in BSCF and BSCF@CeO_2-x (x=10, 20, 30).

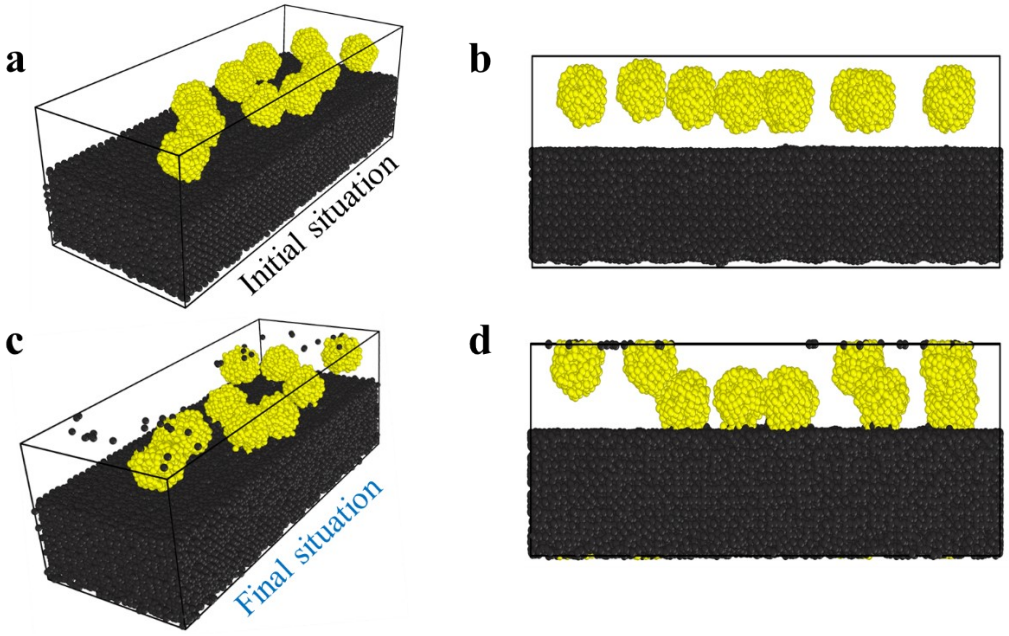

Fig. S6 Molecular dynamics models of BSCF@CeO_2-10 (a) and its longitudinal section (b) at the initial sintering stage. Molecular dynamics models of BSCF@CeO_2-10 (c) and its longitudinal section (d) at the final sintering stage.

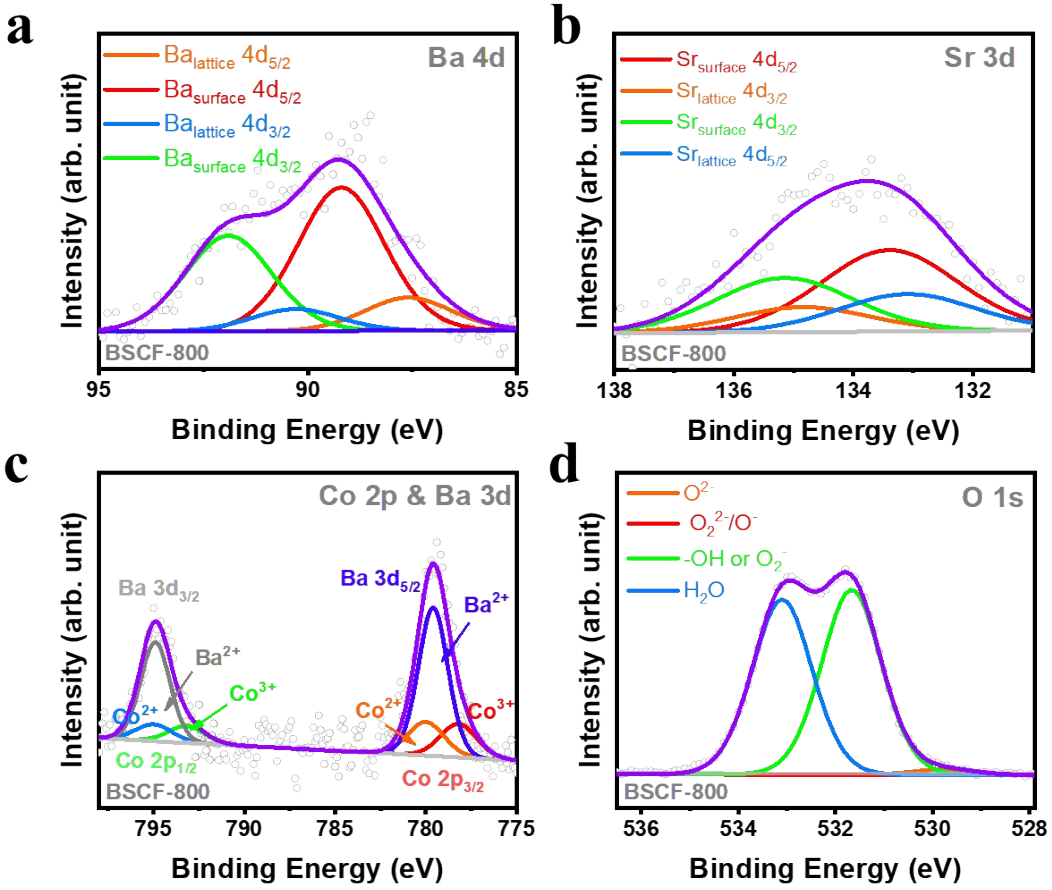

Fig. S7 XPS analysis of (a) Ba 4d, (b) Sr 3d, (c) Co 2p and (d) O 1s in BSCF-800.

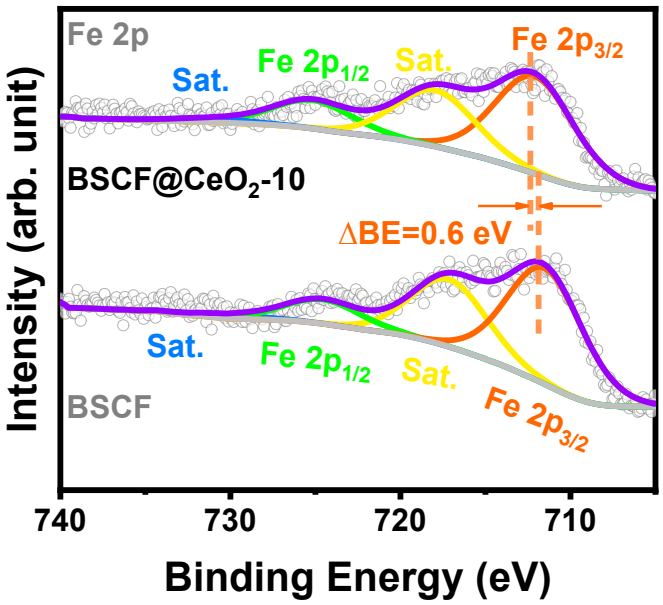

Fig. S8 Fe 2p spectrums in BSCF@CeO_2-10 and BSCF.

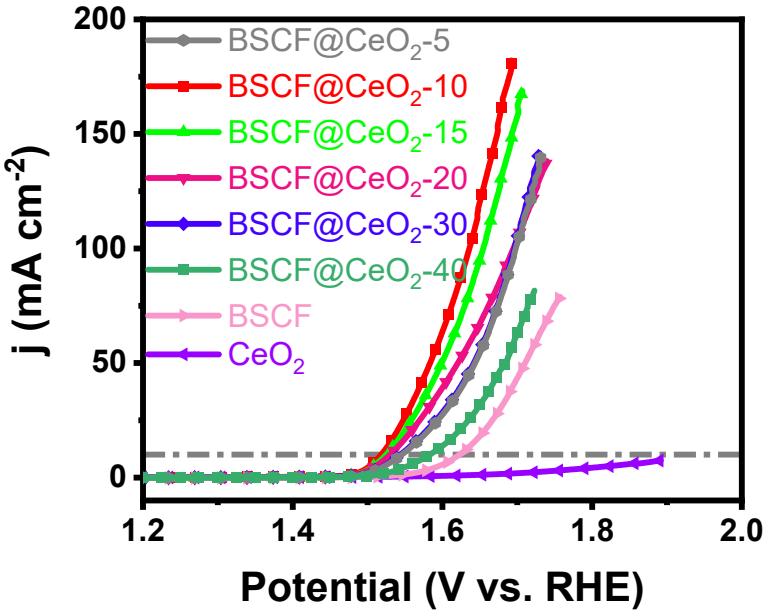

Fig. S9 OER LSV curves of BSCF@CeO_2-x (x=5, 10, 15, 20, 30 and 40), BSCF and CeO_2 in O_2-saturated 1 M KOH.

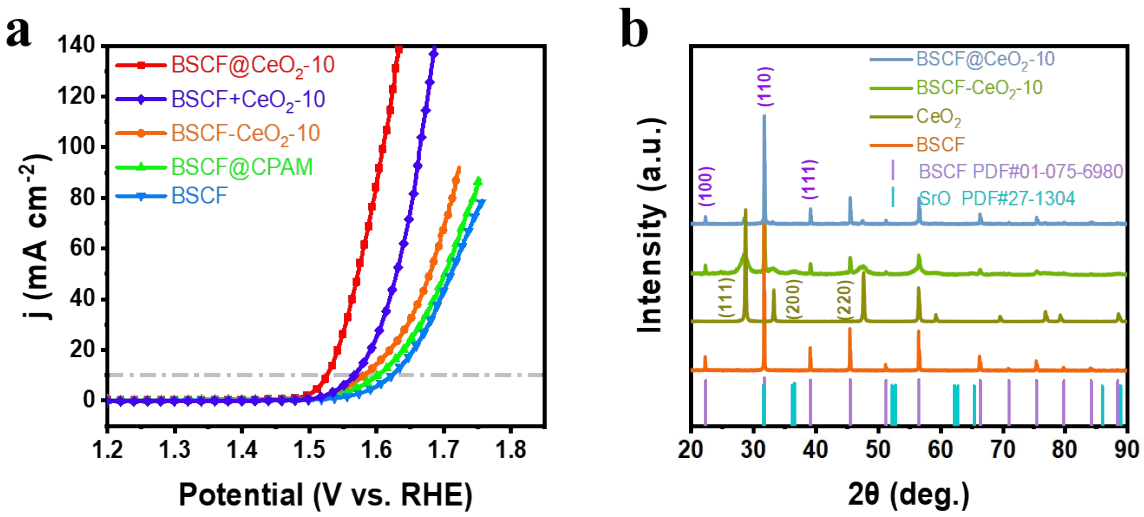

Fig. S10 OER LSV curves of BSCF@CeO_2-10, BSCF+CeO_2-10, BSCF-CeO_2-10, BSCF@CPAM and BSCF in O_2-saturated 1 M KOH (a). XRD patterns of BSCF@CeO_2-10, BSCF-CeO_2-10, CeO_2 and BSCF (b).

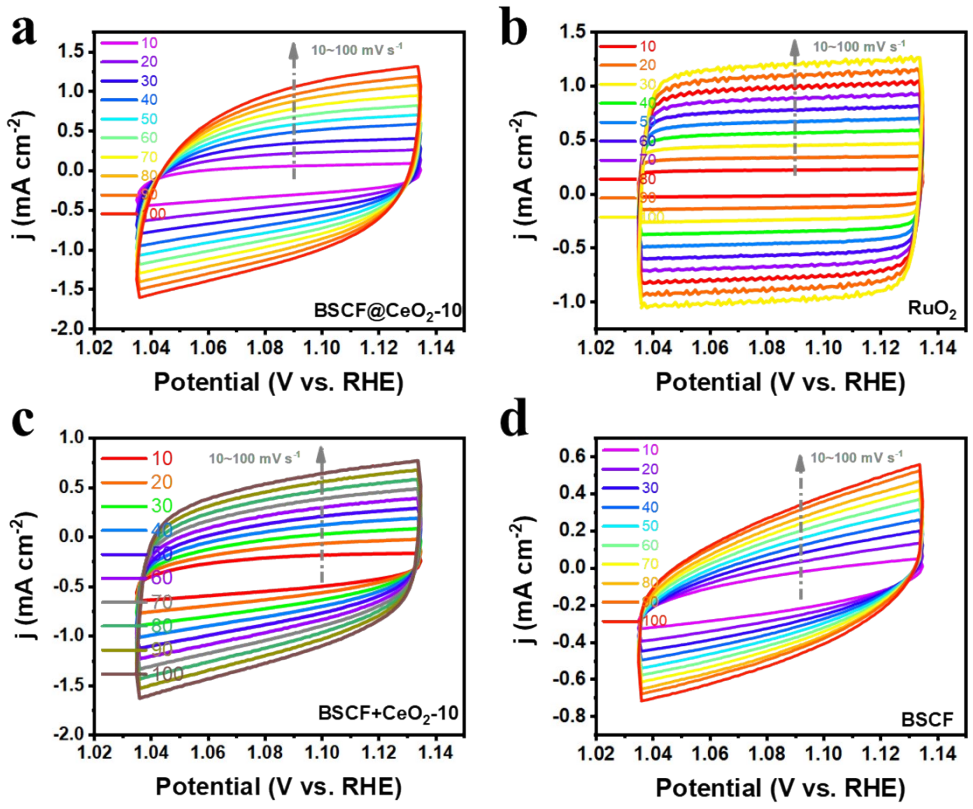

Fig. S11 CV curves of BSCF@CeO_2-10 (a), RuO_2 (b), BSCF+CeO_2-10 (c) and BSCF (d) at different scanning rates (10, 20, 30, 40, 50, 60, 70, 80, 90, 100 mV s^{-1}) in O_2-saturated 1 M KOH.

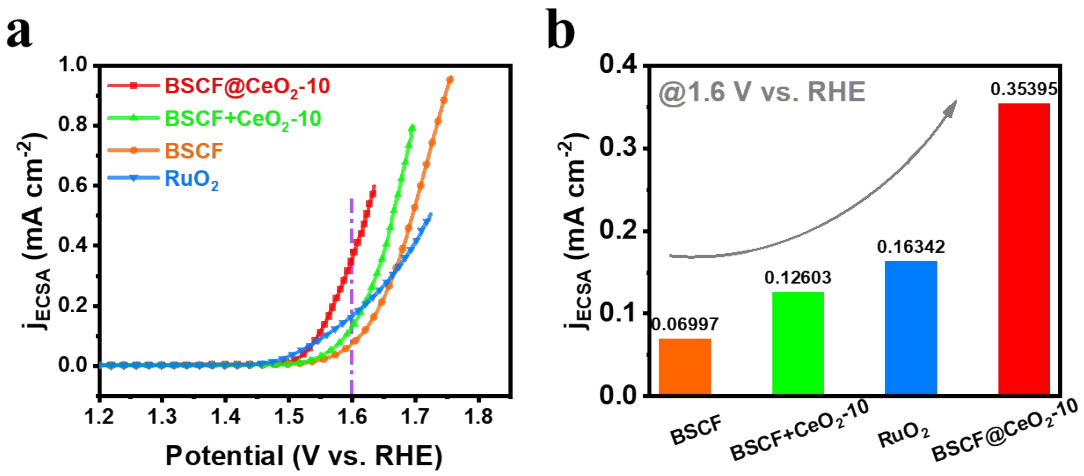

Fig. S12 OER LSV curves (a) and current density (j_{ECSA}) at 1.60 V vs. RHE in OER LSV curves (b) of BSCF@CeO_2-10, RuO_2, BSCF+CeO_2-10 and BSCF normalized by ECSA.

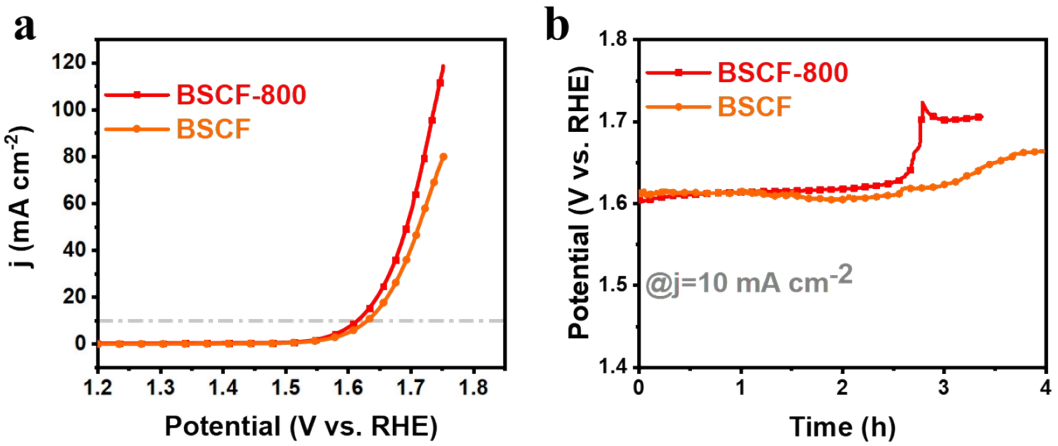

Fig. S13 OER LSV curves of BSCF-800 and BSCF (a). CP tests of BSCF-800 and BSCF at j=10 mA cm^{-2} in O_2-saturated 1 M KOH (b).

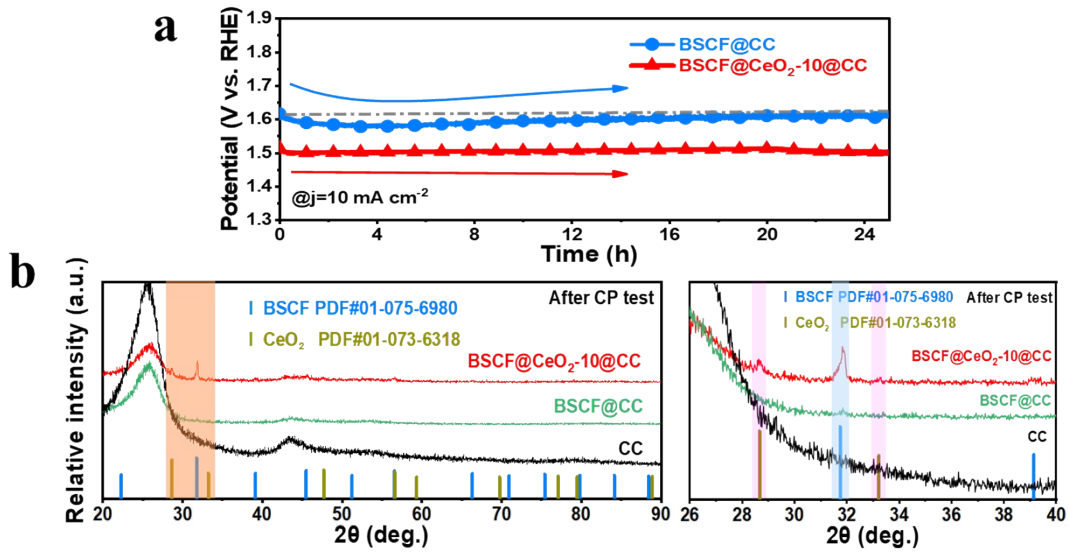

Fig. S14 Chronoamperometry (CP) tests of BSCF@CC and BSCF@CeO_2-10@CC at j=10 mA cm^{-2} for 25 h (a). XRD patterns of BSCF@CC, BSCF@CeO_2-10@CC and their local enlarged images after the 25 h CP test (b).

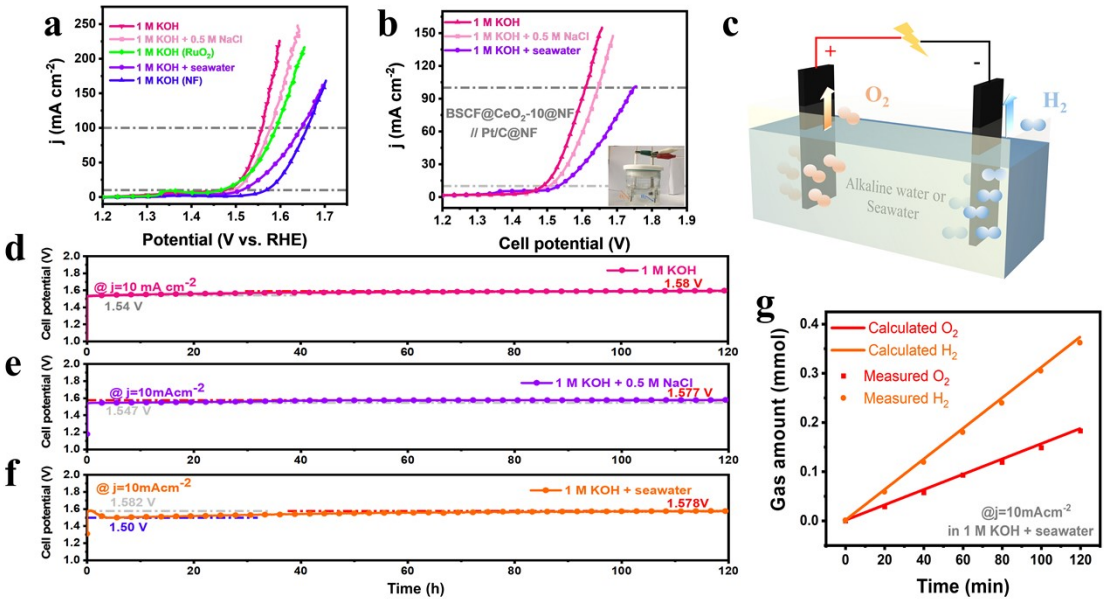

Fig. S15 OER LSV curves of BSCF@CeO_2-10@NF, RuO_2@NF and NF (a), and OWS polarization curves of BSCF@CeO_2-10@NF in 1 M KOH, 1 M KOH + 0.5 M NaCl and 1 M KOH + seawater (Insert is the OWS device) (b). Schematics of OWS for alkaline water and seawater (c). OWS stability tests of BSCF@CeO_2-10@NF in 1 M KOH (d), 1 M KOH + 0.5 M NaCl (e), 1 M KOH + seawater (f) at j=10 mA cm^{-2} for 120 h. Faradaic efficiency measurements of BSCF@CeO_2-10@NF in 1 M KOH + seawater (g) at j=10 mA cm^{-2}.

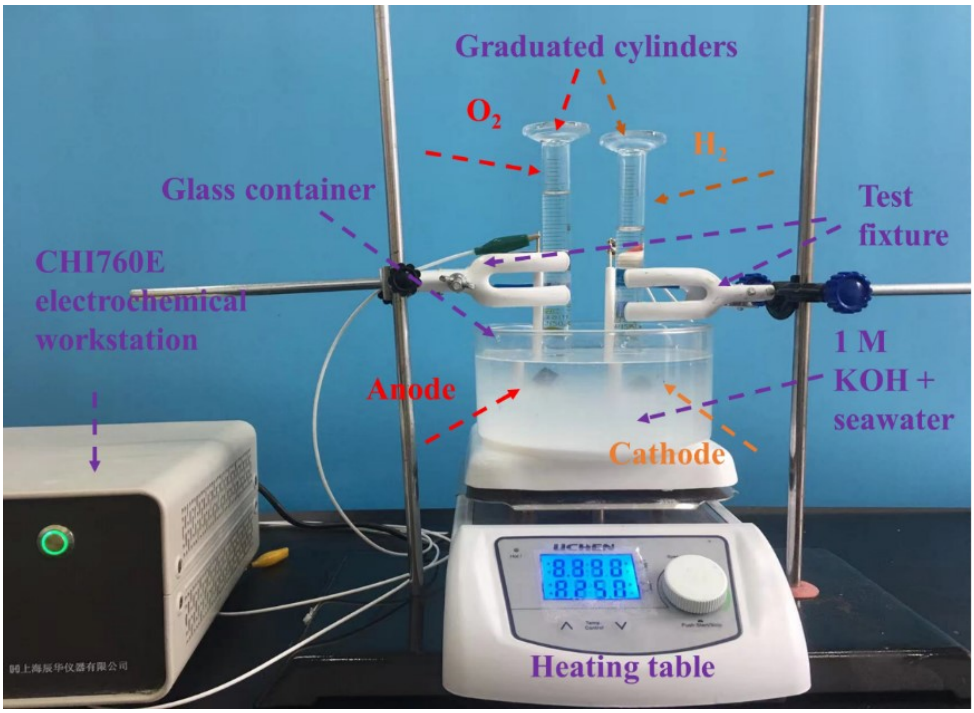

Fig. S16 Diagram of O_2/H_2 Faraday efficiency test device.

Specifically, the gas volume (V_{mea}, mL) of oxygen evolution and hydrogen evolution per 20 min is measured with a graduated cylinder. Then, the corresponding calculation is performed according to the Faraday efficiency (FE) formula:

$$Faraday\ Efficiency = \frac{m \times n \times F}{I \times t}$$

Where the m is the actual number of moles of the product, n is the number of reaction electrons (n = 4 for OER, n = 2 for HER), F is the Faraday constant (F=96485.3383 ± 0.0083 C mol^{-1}), I is current, t is time and the subscript notation $_{mea}$ is 'measured'. The theoretical oxygen evolution and hydrogen evolution Faradaic efficiency is 100 %.

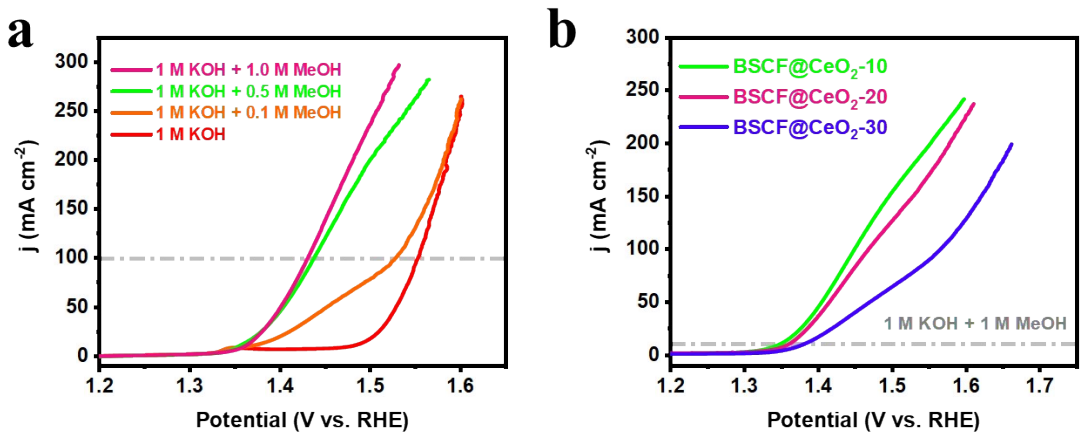

Fig. S17 MOR LSV curves of BSCF@CeO_2-10@NF in N_2-saturated (0, 0.1, 0.5 and 1.0) M MeOH + 1 M KOH solutions (a). MOR LSV curves of BSCF@CeO_2-x (10, 20 and 30)@NF in N_2-saturated 1 M MeOH + 1 M KOH solution (b).

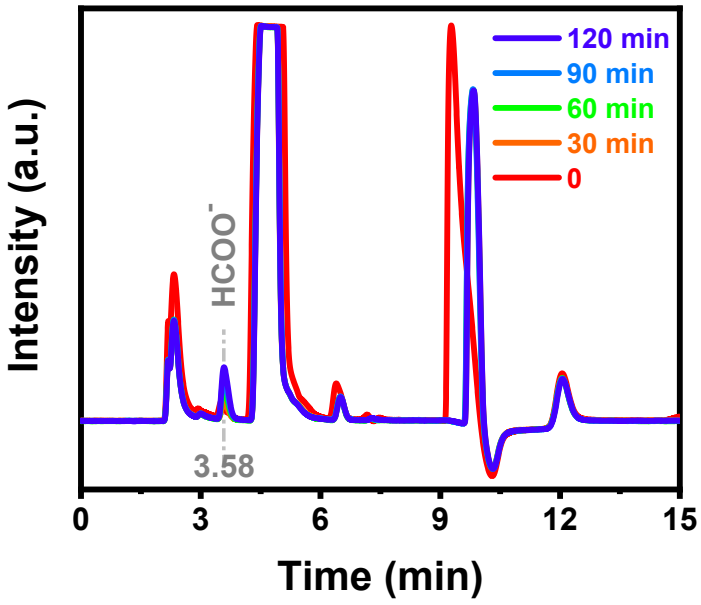

Fig. S18 Ion chromatography (IC) results of the electrolytes after 0 min, 30 min, 60 min, 90 min and 120 min stability test in 1 M KOH + seawater + 1 M MeOH.

The identification and quantification analysis of the formate product are conducted by Ion Chromatography (IC, Thermo Aquion ICS 1100, USA) [8]. The anode electrolytes are analyzed by IC to detect the formate generation after 0, 30, 60, 90, 120 min CP tests.

The identification and quantification of the formate products are determined by calibration curve by applying standard formate solutions with the known concentrations prepared by the commercially purchased pure sodium formate (chromatographic pure). The Faradaic efficiency (FE) of formate generation is calculated using the following equation:

$$FE = \frac{m_{formate}}{It/(4F)} \times 100\ \%$$

$$FE = \frac{4 \times 96485\left(\frac{C}{mol}\right) \times w_t\left(\frac{mg}{L}\right) \times V\ (L) \times 10^{-3}(\frac{g}{mg})}{m_{formate}\ (\frac{g}{mol}) \times \int_0^t I\ (A)dt} \times 100\ \%$$

Among them, F is the Faraday constant (F=96485.3383 ± 0.0083 C mol^{-1}). w_t (mg L^{-1}) is the concentration of formed formate in the solution from the anode compartment. V (L) is the total volume of the solution in the anode compartment of the cell. $m_{formate}$ (g mol^{-1}) is the molecular weight of formate ($HCOO^-$). I (A) is the current recorded by the electrochemical workstation in the chronoamperometry (I-t) mode.

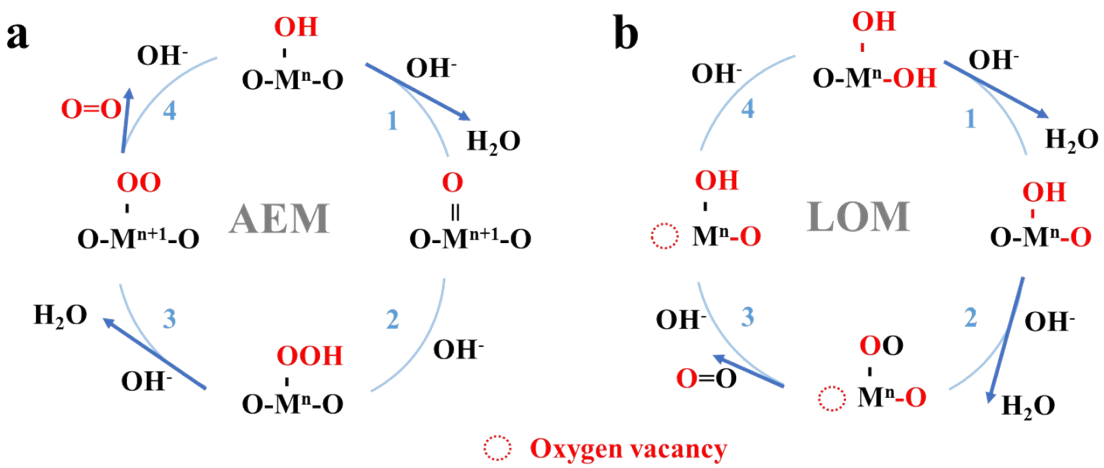

Fig. S19 OER routes of the adsorbate evolution mechanism (AEM) (a) and lattice oxygen oxidation mechanism (LOM) (b).

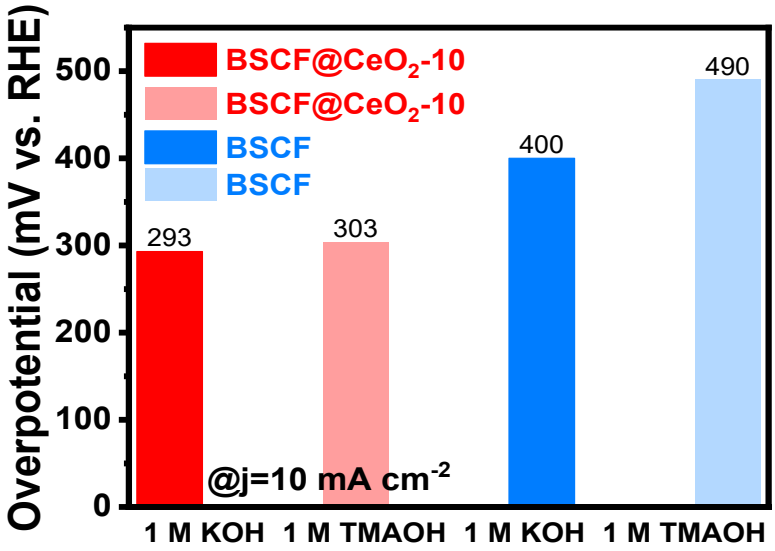

Fig. S20 The corresponding overpotentials of BSCF@CeO_2-10 and BSCF in 1 M KOH and 1 M TMAOH at j=10 mA cm^{-2}, respectively.

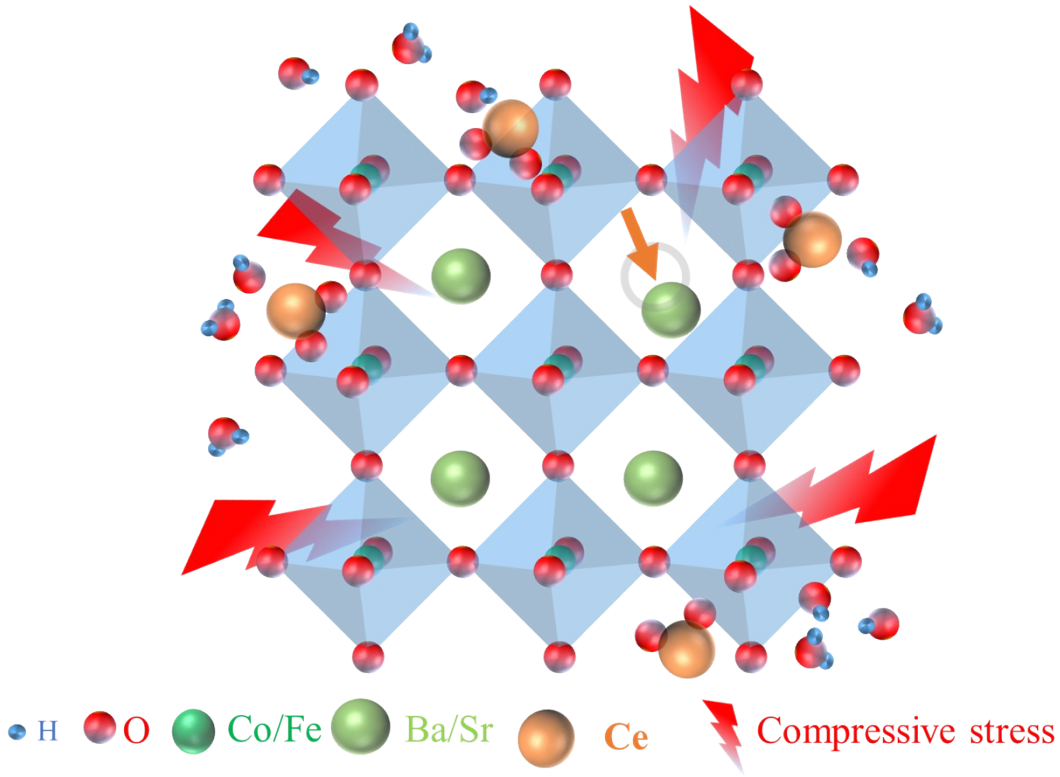

Fig. S21 Effecting mechanism of CeO_2 on BSCF in BSCF@CeO_2-10.

Tab. S1. Lattice parameters and volumes of BSCF phase in BSCF and BSCF@CeO_2-x (x=5, 10, 15, 20, 30, 40) from XRD refinement results.

Sample	a (Å)	b (Å)	c (Å)	unit cell volume (V, $Å^3$)
BSCF	3.982128	3.982128	3.982128	63.15
BSCF@CeO_2-5	3.972347	3.972347	3.972347	62.68
BSCF@CeO_2-10	**3.9714**	**3.9714**	**3.9714**	**62.64**
BSCF@CeO_2-15	3.967444	3.967444	3.967444	62.45
BSCF@CeO_2-20	3.960307	3.960307	3.960307	62.11
BSCF@CeO_2-30	3.962152	3.962152	3.962152	62.2
BSCF@CeO_2-40	3.964626	3.964626	3.964626	62.32

Tab. S2. Molecular dynamics simulation results of BSCF@CeO_2-10.

Samples	Start (abc/Å)	End (abc/Å)	relative change (%)
BSCF phase in BSCF@CeO_2-10	4.010	3.739	6.76

Tab. S3. XPS quantitative analyses (atomic percentages) of the major elements in BSCF-800, BSCF, CeO_2 and BSCF@CeO_2-10.

Sample	Sr suface	Sr lattice	Ba sufface	Ba lattice	Co^{3+}	Co^{2+}	Co^{3+}/Co^{2+}	Ba^{2+}	O^{2-}	O_2^{2-}/O^-	-OH or O_2	H_2O
BSCF-800	68.52	31.48	81.22	18.78	16.78	16.81	1.0	66.41	1.59	~0	50.54	47.87
BSCF	50.38	49.62	83.52	16.48	27.3	27.53	0.99	45.17	23.74	64.47	5.29	6.50
CeO_2				/					56.44	22.49	12.11	8.96
BSCF@CeO_2-10	40.83	59.17	83.38	16.62	37.91	17.08	2.22	45.01	17.49	39.58	22.31	20.63

Tab. S4. XPS quantitative analyses (atomic percentages) of the major elements in CeO_2 and BSCF@CeO_2-10.

Sample	Ce^{3+}	Ce^{4+}
CeO_2	20.85	79.15
BSCF@CeO_2-10	45.58	54.42

Tab. S5. OER performance comparison of BSCF@CeO_2-10 in this work with other Co-based perovskites.

Sample	$E_{j=10}$ (V)	Tafel slope (mV dec^{-1})	$E_{j=50}$ (V)	Electrolyte	Substrate	Reference
BSCF@CeO_2-10	1.52	65.03	1.58	1 M KOH	Glassy carbon	This work
BSCF+CeO_2-10	1.57	78.84	1.63	1 M KOH	Glassy carbon	
BSCF	1.63	88.97	1.71	1 M KOH	Glassy carbon	
CeO_2	/*	374.56	/	1 M KOH	Glassy carbon	
LBSCOF	~1.62	~113	~1.70	1 M KOH	Glassy carbon	[9]
SNCF-NRs	1.60	48	~1.65	1 M KOH	Glassy carbon	[10]
3C-$SrIrO_3$	1.54	74	~1.67	1 M KOH	Glassy carbon	[11]
S-LCF	1.59	60	~1.68	1 M KOH	Glassy carbon	[12]
$CaCoO_3$	~1.56	N. A.	~1.60	1 M KOH	Glassy carbon	[13]
$SrCoO_3$	~1.57	N. A.	~1.61	1 M KOH	Glassy carbon	
$LaCoO_3$	1.78	N. A.	/	1 M KOH	Glassy carbon	
Ir/CeO_2	1.53	44.3	1.60	1 M KOH	Glassy carbon	[14]
$PrBaCo_{0.8}W_{0.2}$	1.55	79.33	1.61	1 M KOH	Glassy carbon	[15]
BSCF	1.56	119.73	/	1 M KOH	Glassy carbon	[16]
IrO_2	1.58	81	~1.67	1 M KOH	Glassy carbon	[17]
$LaCoO_3$/MoS_2−4 (2H)	1.60	62.5	1.67	1 M KOH	Glassy carbon	[18]

Co/SFM-P	1.536	41.9	~1.62	1 M KOH	Glassy carbon	[19]

*: / = Not available.

Tab. S6. MOR performance comparison of this work with the other materials.

Sample	Electrolyte	$E_{j=10}$ (V)	Tafel slope (mV dec^{-1})	$E_{j=50}$ (V)	Scan rate (mV s^{-1})	Reference
BSCF@CeO_2-10	**1 M KOH+1 M MeOH**	**1.39 (0.47 vs. Hg/HgO)**	**101.38**	**1.48 (0.56 vs. Hg/HgO)**	**5**	**This work**
BSCF	1 M KOH+1 M MeOH	1.50	103.36	1.60	5	
CeO_2	1 M KOH+1 M MeOH	/*	172.96	/	5	
BSCF@CeO_2-10 @NF	1 M KOH+1 M MeOH	1.35	/	1.40	5	
$La_{1.4}Sr_{0.6}NiO_{4+\delta}$	0.5 M NaOH+1.5 M MeOH	/	/	/	50	[20]
NiSe/RGO-550	1 M NaOH+0.5 M MeOH	1.42	/	1.68	5	[21]
NiO NTs-400	1 M NaOH+0.5 M MeOH	1.44	82	1.60	50	[22]
$AgNi_{0.8}Co_{0.2}O_2$	1 M KOH+1 M MeOH	1.43	52.6	1.56	50	[23]
NiB-400	1 M KOH+1 M MeOH	~1.40	/	~1.47	5	[24]
$Ni_{2.5}Co_{0.5}Sn_2$	1 M KOH+2 M MeOH	0.45 vs. Hg/HgO	/	0.57 vs. Hg/HgO	50	[25]

*: / = Not available.

Tab. S7. Oxygen ion diffusion coefficients of BSCF@CeO_2-10, BSCF and CeO_2.

Sample	Oxygen ion diffusion coefficients (D_O, $cm^2\ s^{-1}$)
BSCF@CeO_2-10	**9.263×10^{-6}**
BSCF	1.559×10^{-8}
CeO_2	1.169×10^{-13}

Reference:

[1] X. Wu, H. Miao, M. Yin, R. Hu, F. Wang, H. Zhang, L. Xia, C. Zhang, J. Yuan, Biomimetic construction of bifunctional perovskite oxygen catalyst for zinc-air batteries, Electrochimica Acta, 399 (2021) 139407.

[2] Q. Han, Y. Luo, J. Li, X. Du, S. Sun, Y. Wang, G. Liu, Z. Chen, Efficient NiFe-based Oxygen Evolution Electrocatalysts and Origin of their Distinct Activity, Applied Catalysis B: Environmental, 304 (2022) 120937.

[3] S. Dresp, F. Dionigi, M. Klingenhof, P. Strasser, Direct Electrolytic Splitting of Seawater: Opportunities and Challenges, ACS Energy Letters, 4 (2019) 933-942.

[4] Y. Zhu, Q. Lin, Z. Hu, Y. Chen, Y. Yin, H.A. Tahini, H.J. Lin, C.T. Chen, X. Zhang, Z. Shao, H. Wang, Self-Assembled Ruddlesden-Popper/Perovskite Hybrid with Lattice-Oxygen Activation as a Superior Oxygen Evolution Electrocatalyst, Small, 16 (2020) e2001204.

[5] Y. Pan, X. Xu, Y. Zhong, L. Ge, Y. Chen, J.-P.M. Veder, D. Guan, R. O'Hayre, M. Li, G. Wang, H. Wang, W. Zhou, Z. Shao, Direct evidence of boosted oxygen evolution over perovskite by enhanced lattice oxygen participation, Nature Communications, 11 (2020) 2002.

[6] S. Plimpton, Fast Parallel Algorithms for Short-Range Molecular Dynamics, Journal of Computational Physics, 117 (1995) 1-19.

[7] P J. Mitchell, D. Fincham, Shell model simulations by adiabatic dynamics, Journal of Physics: Condensed Matter, 5 (1993) 1031.

[8] S. Li, R. Ma, J. Hu, Z. Li, L. Liu, X. Wang, Y. Lu, G.E. Sterbinsky, S. Liu, L. Zheng, J. Liu, D. Liu, J. Wang, Coordination environment tuning of nickel sites by oxyanions to optimize methanol electro-oxidation activity, Nature Communications, 13 (2022) 2916.

[9] B. Hua, M. Li, W. Pang, W. Tang, S. Zhao, Z. Jin, Y. Zeng, B. Shalchi Amirkhiz, J.-L. Luo, Activating p-Blocking Centers in Perovskite for Efficient Water Splitting, Chem, 4 (2018) 2902-2916.

[10] Y. Zhu, W. Zhou, Y. Zhong, Y. Bu, X. Chen, Q. Zhong, M. Liu, Z. Shao, A Perovskite Nanorod as Bifunctional Electrocatalyst for Overall Water Splitting, Advanced Energy Materials, 7 (2017) 1602122.

[11] X. Ye, S. Song, L. Li, Y.-C. Chang, S. Qin, Z. Liu, Y.-C. Huang, J. Zhou, L.-j. Zhang, C.-L. Dong, C.-W. Pao, H.-J. Lin, C.-T. Chen, Z. Hu, J.-Q. Wang, Y. Long, A'–B Intersite Cooperation-Enhanced Water Splitting in Quadruple Perovskite Oxide $CaCu_3Ir_4O_{12}$, Chemistry of Materials, 33 (2021) 9295-9305.

[12] L. Tang, Z. Chen, F. Zuo, B. Hua, H. Zhou, M. Li, J. Li, Y. Sun, Enhancing perovskite electrocatalysis through synergistic functionalization of B-site cation for efficient water splitting, Chemical Engineering Journal, 401 (2020) 126082.

[13] X. Li, H. Wang, Z. Cui, Y. Li, S. Xin, J. Zhou, Y. Long, C. Jin, J.B. Goodenough, Exceptional oxygen evolution reactivities on $CaCoO_3$ and $SrCoO_3$, Science advances, 5 (2019) eaav6262.

[14] K. Xu, Z. Zhu, W. Guo, H. Zhang, T. Yu, W. Wei, W. Liang, D. Zhang, M. He, T. Yang, Cerium oxide modified iridium nanorods for highly efficient electrochemical water splitting, Chemical Communications, 57 (2021) 8798-8801.

[15] J. Yan, M. Xia, C. Zhu, D. Chen, F. Du, Perovskite With Tunable Active-Sites Oxidation State by High-Valence W for Enhanced Oxygen Evolution Reaction, Frontiers in chemistry, 9 (2021) 809111.
[16] J. Xiong, H. Zhong, J. Li, X. Zhang, J. Shi, W. Cai, K. Qu, C. Zhu, Z. Yang, S.P. Beckman, H. Cheng, Engineering highly active oxygen sites in perovskite oxides for stable and efficient oxygen evolution, Applied Catalysis B: Environmental, 256 (2019) 117817.
[17] N.K. Oh, J. Seo, S. Lee, H.J. Kim, U. Kim, J. Lee, Y.K. Han, H. Park, Highly efficient and robust noble-metal free bifunctional water electrolysis catalyst achieved via complementary charge transfer, Nature Communications, 12 (2021) 4606.
[18] A.K. Rana, M.H. Jeong, Y.I. Noh, H. Park, J.M. Baik, K.J. Choi, Phase-Tuned MoS_2 and Its Hybridization with Perovskite Oxide as Bifunctional Catalyst: A Rationale for Highly Stable and Efficient Water Splitting, ACS Applied Materials & Interfaces, 14 (2022) 18248-18260.
[19] L. Tan, Z. Jiang, Y. Gao, S. Zhang, Synergistic interaction between in situ exsolved and phosphorized nanoparticles and perovskite oxides for enhanced electrochemical water splitting, International Journal of Hydrogen Energy, 47 (2022) 20016-20026.
[20] P. Chandrasekharan Meenu, P.K. Samanta, T. Yoshida, N.J. English, S.P. Datta, S.A. Singh, S. Dinda, C. Chakraborty, S. Roy, Electro-Oxidation Reaction of Methanol over $La_{2-x}Sr_xNiO_{4+\delta}$ Ruddlesden–Popper Oxides, ACS Applied Energy Materials, 5 (2022) 503-515.
[21] J. Jia, L. Zhao, Y. Chang, M. Jia, Z. Wen, Understanding the growth of NiSe nanoparticles on reduced graphene oxide as efficient electrocatalysts for methanol oxidation reaction, Ceramics International, 46 (2020) 10023-10028.
[22] T.J. Wang, H. Huang, X.R. Wu, H.C. Yao, F.M. Li, P. Chen, P.J. Jin, Z.W. Deng, Y. Chen, Self-template synthesis of defect-rich NiO nanotubes as efficient electrocatalysts for methanol oxidation reaction, Nanoscale, 11 (2019) 19783-19790.
[23] X. Zhang, L. Kong, W. Xing, Y. Zhang, J. Yang, C. Zhou, H. Liu, Z. Yang, W. Zhu, H. Wei, Highly Efficient Methanol Oxidation Reaction Achieved by Cobalt Doping in Delafossite $AgNi_{1-x}Co_xO_2$ Solid Solution, ACS Applied Energy Materials, 5 (2022) 12485-12495.
[24] Y. Qi, Y. Zhang, L. Yang, Y. Zhao, Y. Zhu, H. Jiang, C. Li, Insights into the activity of nickel boride/nickel heterostructures for efficient methanol electrooxidation, Nature Communications, 13 (2022) 4602.
[25] J. Li, Z. Luo, F. He, Y. Zuo, C. Zhang, J. Liu, X. Yu, R. Du, T. Zhang, M.F. Infante-Carrió, P. Tang, J. Arbiol, J. Llorca, A. Cabot, Colloidal Ni–Co–Sn nanoparticles as efficient electrocatalysts for the methanol oxidation reaction, Journal of Materials Chemistry A, 6 (2018) 22915-22924.